

Design and synthesis of three-dimensional hybrid Ruddlesden-Popper nickelate single crystals

Feiyu Li,¹ Ning Guo,² Qiang Zheng,² Yang Shen,³ Shilei Wang,¹ Qihui Cui,¹ Chao Liu,¹ Shanpeng Wang,¹ Xutang Tao,^{1*} Guang-Ming Zhang,^{4,5*} Junjie Zhang^{1*}

¹State Key Laboratory of Crystal Materials and Institute of Crystal Materials, Jinan, Shandong 250100, China

²CAS Key Laboratory of Standardization and Measurement for Nanotechnology, CAS Center for Excellence in Nanoscience, National Center for Nanoscience and Technology, Beijing, 100190 China

³Key Laboratory of Artificial Structures and Quantum Control, School of Physics and Astronomy, Shanghai Jiao Tong University, Shanghai 200240, China

⁴State Key Laboratory of Low-Dimensional Quantum Physics, Department of Physics, Tsinghua University, Beijing, China.

⁵Frontier Science Center for Quantum Information, Beijing 10008, China

*Email: jingt535tao@163.com (X. Tao), gmgzhang@mail.tsinghua.edu.cn (G. M. Zhang), and junjie@sdu.edu.cn (J. Zhang)

Abstract: Advancement of technologies relies on discovery of new materials with emerging physical properties that are determined by their crystal structures. Ruddlesden-Popper (R-P) phases with formula of $A_{n+1}B_nX_{3n+1}$ ($n=1,2,3\dots\infty$) are among one of the most widely studied class of materials due to their electrical, optical, magnetic, thermal properties and their combined multifunctional properties.¹⁻⁶ In R-P phases, intergrowth is well-known in the short range;⁷⁻⁹ however, no existing compounds have been reported to have different n mixed in bulk single crystals. Here we design a hybrid R-P nickelate $\text{La}_2\text{NiO}_4\cdot\text{La}_3\text{Ni}_2\text{O}_7$ by alternatively stacking bilayers, which is the active structural motif in the newly discovery high- T_c superconductor $\text{La}_3\text{Ni}_2\text{O}_7$ and single layers of the antiferromagnetic insulator La_2NiO_4 . We report the successful synthesis of $\text{La}_2\text{NiO}_4\cdot\text{La}_3\text{Ni}_2\text{O}_7$ single crystals, and X-ray diffraction and real-space imaging vis STEM show that the crystal structure consists of single layers and bilayers of NiO_6 octahedral stacking alternatively perpendicular to the ab plane, characterized by the orthorhombic $Immm$ (No.71) space group. Resistivity measurements indicate a peculiar insulator-to-metal transition around 140 K on cooling. Correlated density functional theory (DFT+ U) calculations corroborate this finding, and reveal that the single layer becomes paramagnetic metallic due to charge transfer via LaO layers. The discovery of $\text{La}_2\text{NiO}_4\cdot\text{La}_3\text{Ni}_2\text{O}_7$ opens a door to access a completely new family of 3D hybrid R-P phases with the formula of $A_{n+1}B_nX_{3n+1}\cdot A'_{m+1}B'_mX'_{3m+1}$ ($n\neq m$), which potentially host a plethora of emerging physical properties

for various applications.

Quasi-2D layered R-P oxide perovskites display various emerging physical properties ranging from high temperature superconductivity,^{1,10} colossal magnetoresistance,⁴ metal-insulator transition² and multiferroicity.^{5,11} The ternary oxide system La-Ni-O contains a homologous series of layered phases of general composition (LaO)(LaNiO₃)_n, in which *n* layers of perovskite-type LaNiO₃ are separated by single NaCl-type LaO layers.¹² The average oxidation state of Ni in La_{n+1}Ni_nO_{3n+1} (*n*=1, 2, 3, ..., ∞) varies from 2+ for *n*=1 to 2.5+ for *n*=2 and to 3+ for *n*=∞. The first member of this series, La₂NiO₄, is known to have a tetragonal structure with the rotated NiO₆ octahedrons, being an antiferromagnetic Mott insulator at low temperatures.¹³ Recently, signature of superconductivity with *T_c*~ 80 K above 14 GPa has reported in the second member of this series, the bilayer nickelate La₃Ni₂O₇.¹⁴⁻¹⁷ At ambient pressure, it crystallizes in the orthorhombic *Amam* space group with Ni-O-Ni angle of 168°, and it undergoes a structural transition to *Fmmm* with Ni-O-Ni angle of 180° under high pressure.¹⁴ So there is a nature question whether there exists other high-*T_c* superconducting nickelates at ambient pressure, which share the similar crystal structure of La₃Ni₂O₇ under high pressure. Besides high-*T_c* superconductors, are there any other types of nickelates in which rich physical properties emerge in the electronic phase diagram?

In this paper, we design a new family of perovskites by stacking *n* and *m* layer perovskites in long-range order, yielding three-dimensional A_{n+1}B_nO_{3n+1}·A'_{m+1}B'_mO_{3m+1} hybrid oxide perovskites. As an example, we successfully synthesize single crystals of La₂NiO₄·La₃Ni₂O₇ (*n*=1, *m*=2) for the first time. The key structural motif for the electronic properties in La₃Ni₂O₇ is the bilayer Ni-O planes. On average, each Ni^{2.5+} is half-filled in its 3*d*_{z²} orbital and quarter-filled in its 3*d*_{x²-y²} orbital.¹⁴ Incorporation of the bilayer NiO₂ into a new compound is expected to maintain the key electronic features of La₃Ni₂O₇. In La₂NiO₄, the single-layer NiO₂ planes form a two-dimensional spin-1 Heisenberg antiferromagnetic insulator on a square lattice with a Neel temperature of ~330 K.¹³ Hole doping in La₂NiO₄ results in rich electronic phase diagram, consisting of antiferromagnetic insulator, charge and spin stripes, checkboard charge order and pseudogap.¹⁸ **Fig. 1a** presents our materials design strategy to hybridize bilayer from La₃Ni₂O₇ and single layer from La₂NiO₄ in the long-range order perpendicular to the Ni-O plane. By tailoring La₂NiO₄ into single layers, the antiferromagnetic long-range order is expected to be destroyed and only spin fluctuations are left. The combination of magnetic single layer and superconducting bilayers are predicted to host emerging properties that belong to neither La₂NiO₄ nor La₃Ni₂O₇.

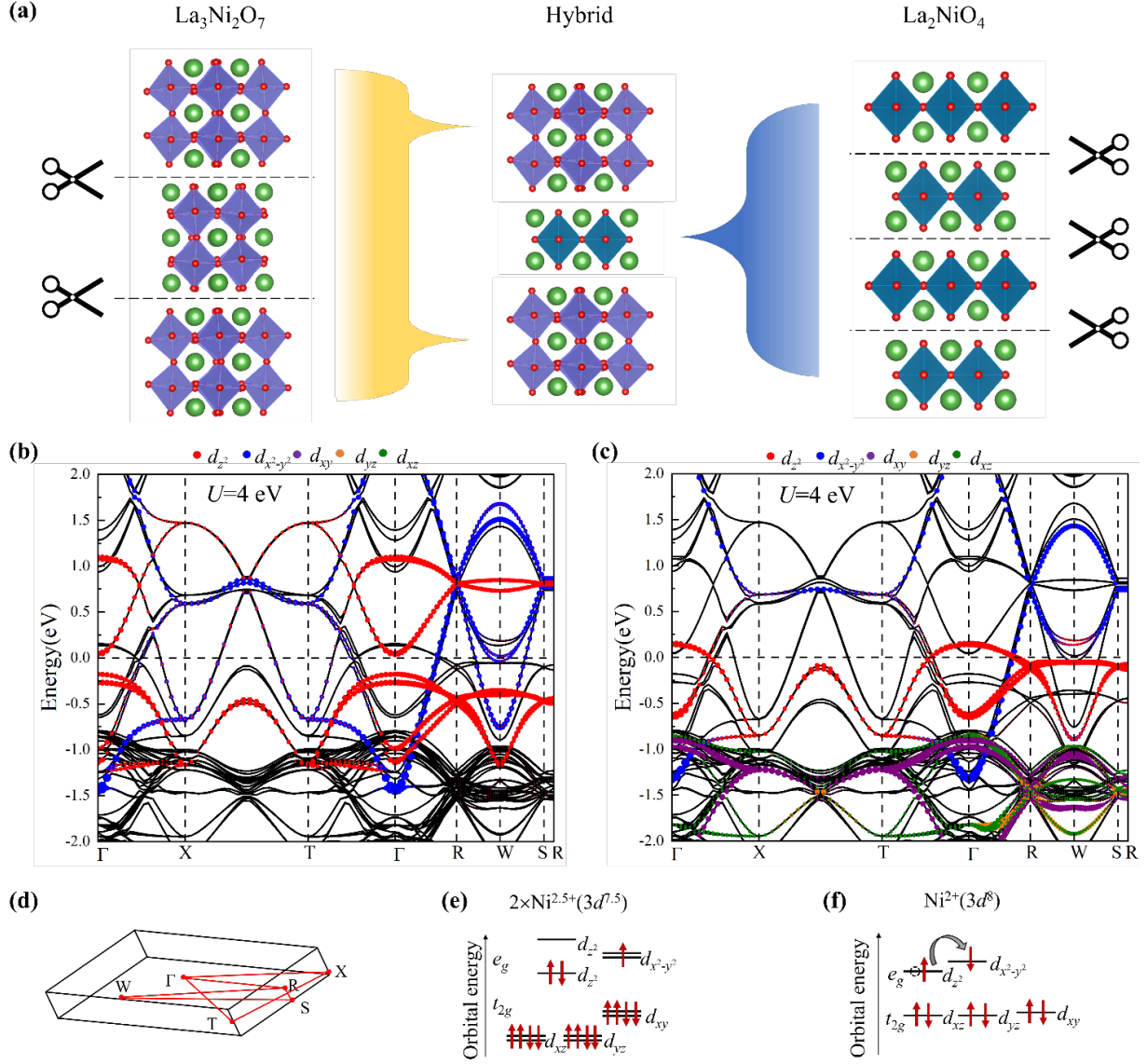


Figure 1. Materials design strategy for hybrid $\text{La}_2\text{NiO}_4 \cdot \text{La}_3\text{Ni}_2\text{O}_7$ and calculated electronic structure. (a) Illustration of our design strategy to hybridize bilayer, the structural motif that is responsible for high-temperature superconductivity in $\text{La}_3\text{Ni}_2\text{O}_7$, and single layer in the 3D antiferromagnetic La_2NiO_4 in the long-range order. (b) Orbital projected weights of the bilayer NiO_2 in the hybrid $\text{La}_2\text{NiO}_4 \cdot \text{La}_3\text{Ni}_2\text{O}_7$ crystal given by the correlated density functional theory. (c) Orbital projected weights of the single NiO_2 in the hybrid $\text{La}_2\text{NiO}_4 \cdot \text{La}_3\text{Ni}_2\text{O}_7$ crystal given by the correlated density functional theory. (d) Schematic of the 3D body-centered orthorhombic Brillouin zone. The red lines correspond to the paths of the electronic bands in (b) and (c). (e) Energy levels of the unit with two $\text{Ni}^{2.5+}$ ($3d^{7.5}$) in the bilayer under the crystal field. The d_{z^2} orbitals of two Ni cations in the neighboring layers form the bonding and anti-bonding states, (f) Energy levels of the unit with Ni^{2+} ($3d^8$) in the single layer under the crystal field. The dotted circle indicates a hole generated by charge transfer from d_{z^2} to $d_{x^2-y^2}$ orbitals.

With this design, we use flux method to synthesize the single crystals of $\text{La}_2\text{NiO}_4 \cdot \text{La}_3\text{Ni}_2\text{O}_7$ at ambient pressure. Conventionally, single crystals of rare earth nickelates with higher nickel valence are prepared either by high oxygen pressure floating zone techniques or high pressure flux method.^{12,19} Recent advancement in growing single crystals of trilayer $\text{La}_4\text{Ni}_3\text{O}_{10}$ has been achieved without high pressure, i.e., single crystals can be prepared at ambient pressure using K_2CO_3 as a flux.²⁰ By changing the initial molar ratio of La and Ni to 5:3, single crystals of $\text{La}_2\text{NiO}_4 \cdot \text{La}_3\text{Ni}_2\text{O}_7$ with dimensions up to 120 μm in length and 80 μm in thickness were prepared. **Fig. 2a** presents the SEM image of a typical single crystal with sizes of $110 \times 80 \times 50 \mu\text{m}^3$ (more crystals are shown in **Fig. S1**). The regular shape with smooth and clean surface of the sample indicates high quality of the as-grown single crystal. EDS measurements on single crystals result in La:Ni of 1.77 (sample 1) and 1.70 (sample 2), consistent with the expected 5:3 for $\text{La}_2\text{NiO}_4 \cdot \text{La}_3\text{Ni}_2\text{O}_7$.

The crystal structure at room temperature was determined using in-house X-ray single crystal diffraction. Initial unit cell determination resulted in a unit cell with $c \sim 16.5 \text{ \AA}$, which lies in the middle of La_2NiO_4 with $c \sim 12.7 \text{ \AA}$ ²¹ and $\text{La}_3\text{Ni}_2\text{O}_7$ with $c \sim 20.5 \text{ \AA}$.¹⁴ This observation strongly suggests that it is a long-range intergrowth of single layer and bilayer NiO_2 planes. Subsequent analysis (**Fig. S2**) leads to orthorhombic body centered unit cell with lattice parameters of $a = 5.4296(2) \text{ \AA}$, $b = 5.4330(2) \text{ \AA}$ and $c = 33.2067(12) \text{ \AA}$. **Figs. 2b & 2c** display selected high-symmetry reciprocal lattice planes ($hk0$) and ($h0l$) reconstructed from a total of 2728 frames. The observed peaks obey the selection rule of $h+k+l=\text{even}$, consistent with the body centered unit cell. The structure was solved using the *Immm* (No.71) space group, and the refinements converged to $R_1 = 6.05\%$ and $wR_2 = 10.23\%$. **Fig. S3** shows the observed structural factor F as a function of the calculated values. Ideally the calculated F equals to the observed F as indicated by the red line. Details of crystal parameters, data collection, and structure refinement are summarized in **Table S1**.

Fig. 2d presents the crystal structure of $\text{La}_2\text{NiO}_4 \cdot \text{La}_3\text{Ni}_2\text{O}_7$ using the ball-and-stick model. The unit cell contains two bilayers and two single-layers. The asymmetric unit consists of six La atoms, three Ni atoms and eight O atoms. The La atoms are surrounded by nine or thirteen oxygen atoms with bond length in the range of $2.28(5) - 2.778(11) \text{ \AA}$. The Ni atoms are bonded to six oxygen atoms with bond length of $1.916(10) - 2.227(18) \text{ \AA}$ for the bilayer (**Fig. 2e**) and $1.92026(5) - 2.34(5) \text{ \AA}$ for the single layer (**Fig. 2f**). The Ni-O bond distance along c axis for the bilayer is 3% - 6.5% longer than that of $\text{La}_3\text{Ni}_2\text{O}_7$ or $\text{La}_2\text{PrNi}_2\text{O}_7$ measured at 14-15 GPa.^{14,22} The out-of-plane Ni-O-Ni angle within the bilayer is 180° (**Fig. 2e**), as the same as that of $\text{La}_3\text{Ni}_2\text{O}_7$ in the superconducting state under high pressure.¹⁴ These crystallographic data suggest that $\text{La}_2\text{NiO}_4 \cdot \text{La}_3\text{Ni}_2\text{O}_7$ is a potential material for exploring high temperature superconductivity.

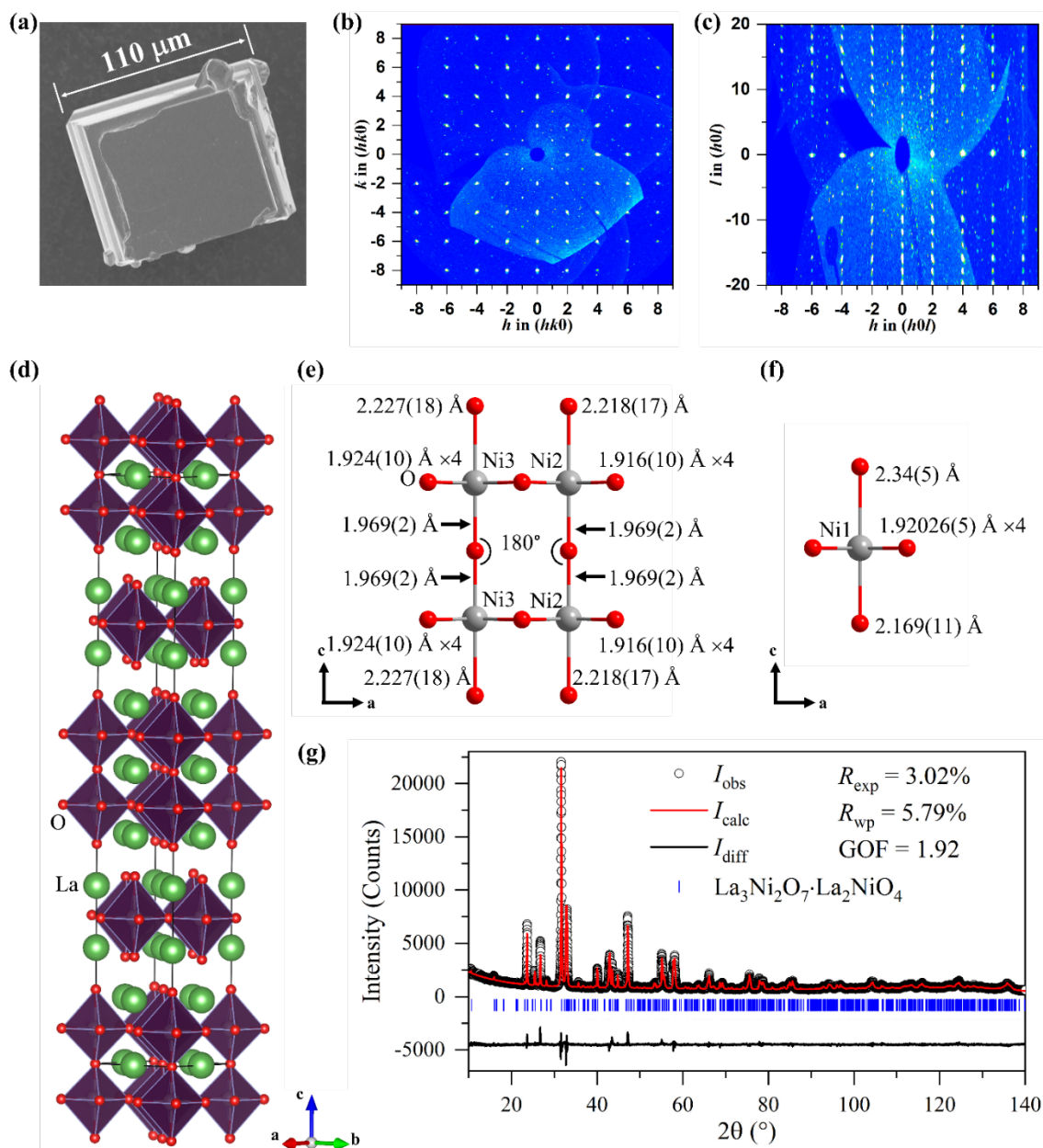


Figure 2. Crystal structure of the single-layer and bilayer hybridized nickelate $\text{La}_2\text{NiO}_4 \cdot \text{La}_3\text{Ni}_2\text{O}_7$. (a) A SEM image of an as-grown single crystal with dimensions of $110 \times 80 \times 50 \mu\text{m}^3$. (b) Reconstructed $(hk0)$ planes from in-house X-ray single crystal diffraction data collected at $296(2) \text{ K}$. (c) Reconstructed $(h0l)$ planes from in-house X-ray single crystal diffraction data collected at $296(2) \text{ K}$. (d) Structural model obtained from X-ray single crystal diffraction. (e) Ball-and-stick drawings of the NiO_6 octahedrons with bond distances and bond angles in the bilayer NiO_2 . (f) Ball-and-stick drawing of the NiO_6 octahedrons with bond distances in the single layer NiO_2 . (g) Rietveld refinement on powder diffraction data collected on pulverized single crystals obtained from flux growth. Structural model in (d) was used as a starting model.

Rietveld refinement on powder diffraction data using the single crystal model was carried out to verify our structural model (**Fig. 2g**). The refinement converged to the following figures of merit: $R_{\text{exp}}=3.02\%$, $R_{\text{wp}}=5.79\%$, and $\text{GOF}=1.92$ with lattice parameters of $a= 5.41730(9) \text{ \AA}$, $b= 5.45820(9) \text{ \AA}$, $c= 33.1844(6) \text{ \AA}$. These reasonable parameters and the small difference between calculated and observed intensity strongly support the crystal structure from single crystal diffraction. We found that there exists a small amount of $\text{La}_3\text{Ni}_2\text{O}_7$ (6.7 wt %) impurity (not shown in the figure) with the rest 93.3 wt % attributable to $\text{La}_2\text{NiO}_4 \cdot \text{La}_3\text{Ni}_2\text{O}_7$. The powders were prepared by pulverizing crystals that previously did not pass through 300-mesh sieves (crystals $>50 \mu\text{m}$ on edge). There exist two possibilities for the source of the impurity: (1) single crystals of $\text{La}_3\text{Ni}_2\text{O}_7$, and (2) inclusions or intergrowth of $\text{La}_3\text{Ni}_2\text{O}_7$ on $\text{La}_2\text{NiO}_4 \cdot \text{La}_3\text{Ni}_2\text{O}_7$. We performed single crystal X-ray diffraction experiments multiple times to select $\text{La}_2\text{NiO}_4 \cdot \text{La}_3\text{Ni}_2\text{O}_7$ single crystals, and we occasionally picked up $\text{La}_3\text{Ni}_2\text{O}_7$ single crystals. By further considering the clean single crystal diffraction pattern and STEM results (shown below), the first source is likely the case. It is difficult to distinguish $\text{La}_2\text{NiO}_4 \cdot \text{La}_3\text{Ni}_2\text{O}_7$ from $\text{La}_3\text{Ni}_2\text{O}_7$ single crystals using microscope due to their similar morphology.

To further verify the long-range intergrowth of single layer and bilayer NiO_2 planes, real-space imaging via STEM was performed. A typical HAADF-STEM image in the $[110]$ projection shown in **Fig. 3a** and a lower-magnification HAADF image shown in **Fig. S4** indicate perfectly ordered stacking of the alternating bilayers and single layers in the length scale of tens of nanometers in the $\text{La}_2\text{NiO}_4 \cdot \text{La}_3\text{Ni}_2\text{O}_7$ single crystals. Such a long-range ordered stacking can be revealed by chemical distributions of La and Ni from EDS maps in **Fig. 3b**. As shown in **Fig. S5** and **Fig. S6**, the HAADF-STEM imaging was also performed along the $[100]$ zone axis, further confirming the fully ordering sequences of the alternating bilayers and single layers.

Fig. 3c shows the magnetic susceptibility of the as-grown $\text{La}_2\text{NiO}_4 \cdot \text{La}_3\text{Ni}_2\text{O}_7$ single crystals in the temperature range of 25-350 K under an external magnetic field of 0.4 T. Between 25 and ~ 200 K, it exhibits the Curie-Weiss behavior, indicating the presence of weakly interacting local magnetic moments. Above ~ 200 K, the magnetic susceptibility is almost temperature independent, consistent with Pauli paramagnetism. The data (not shown) between 2 and 25 K does not show any magnetic long-range order but strong sample dependent. **Fig. 3d** displays the resistivity of polycrystalline pellet of $\text{La}_2\text{NiO}_4 \cdot \text{La}_3\text{Ni}_2\text{O}_7$ pulverized from single crystals and sintered at $900 \text{ }^\circ\text{C}$ in air. In addition to the expected metal-insulator transition at high temperature above 350 K, a peculiar insulator to metal transition occurs around 140 K on cooling, in sharp contrast to the other R-P nickelates such as the insulating behavior of La_2NiO_4 at low temperatures,¹³ the metal-to-metal transition in bilayer $\text{La}_3\text{Ni}_2\text{O}_7$ and trilayer $\text{La}_4\text{Ni}_3\text{O}_{10}$,²³⁻²⁵ and the metal-to-insulator transition in RNiO_3 (R=Pr - Lu, Y).²⁶ The

underlying physics of this insulator-to-metal transition may be related to the presence of charge transfer between insulating single layer and metallic bilayers in this hybrid structure.

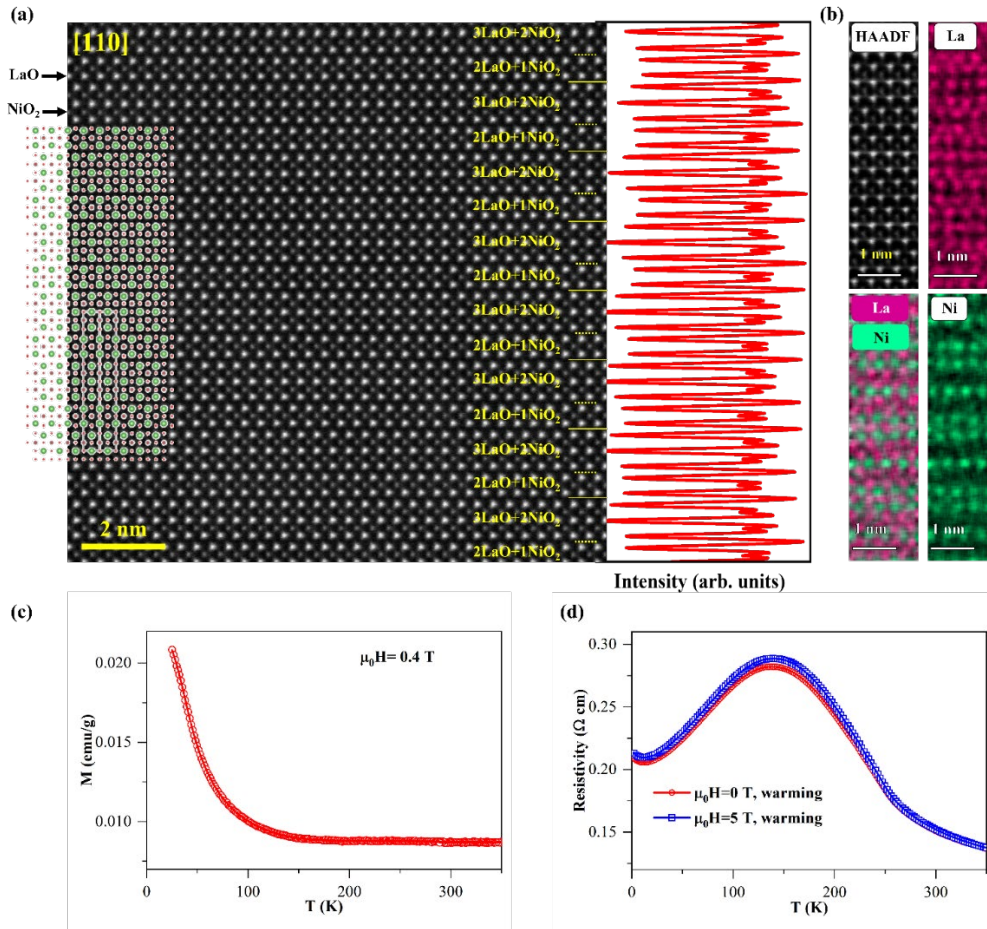


Figure 3. Real-space imaging of the structure and physical properties of $\text{La}_3\text{Ni}_2\text{O}_7 \cdot \text{La}_2\text{NiO}_4$. (a) A typical atomic-scale HAADF-STEM image in the projection of [110] with overlaid crystal structure model; the right panel is line intensity profile for rows of all atomic columns. (b) EDS maps for La and Ni and mixed color map of them. (c) Magnetic susceptibility of as-grown single crystals. (d) Resistivity on warming under an external magnetic field of 0 and 5 T. Note a single crystal is too small to put four leads on, polycrystalline pellets were used and treated at 900 °C in air prior to making contacts.

With the determined structure of single crystals and low-temperature physical properties, we performed the numerical calculation of correlated density functional theory (DFT+ U) for the single crystal $\text{La}_2\text{NiO}_4 \cdot \text{La}_3\text{Ni}_2\text{O}_7$ within a non-magnetic solution. With an intermediate on-site Coulomb interaction $U=4$ eV, we find that the electronic states near the Fermi level are dominated by the Ni $3d_{x^2-y^2}$ and $3d_{z^2}$ orbitals in the energy window of -2 eV to 2 eV, while the Ni t_{2g} orbital electrons are far below the Fermi energy (Fig. S7). The Ni $3d_{z^2}$ orbitals are mixed with oxygen $2p_z$ orbitals across the

Fermi level, indicating strong covalent hybridization among these orbitals (**Fig. S7**). The rare-earth element La has little hybridization with Ni and O $2p_z$ orbitals (**Fig. S8**). Actually, it had better to present complementary plots of the Ni e_g bands disentangled according to their origin from Ni sites in the different structural units. **Fig. 1b** displays the orbital projected weights of the structural units with NiO_6 octahedral bilayers in the hybrid $\text{La}_2\text{NiO}_4 \cdot \text{La}_3\text{Ni}_2\text{O}_7$ crystal, where the $3d_{z^2}$ orbitals form the σ -bonding and anti-bonding bands via the inter-layer apical oxygens, opening a small energy gap at the Fermi energy (**Fig. 1d**). This gives rise to the half-filled $3d_{z^2}$ orbitals and the quarter filled $3d_{x^2-y^2}$ orbitals, very similar to the electronic structure of $\text{La}_3\text{Ni}_2\text{O}_7$.¹⁴ However, the orbital projected weights of the structural units with NiO_6 octahedral single layers in the hybrid $\text{La}_2\text{NiO}_4 \cdot \text{La}_3\text{Ni}_2\text{O}_7$ crystal show that the $3d_{x^2-y^2}$ electrons are nearly free with parabolic dispersions along the Γ -R direction, the $3d_{z^2}$ orbital band is hole doped with a narrow bandwidth, and the van Hove singularity of correlated $3d_{z^2}$ electrons along the R-S direction may induce a possible electronic instability (**Fig. 1c**). These numerical results can be simplified as shown in **Figs. 1e & 1f**, and are consistent with the paramagnetic metallic behavior observed in the low-temperature experimental result.

Therefore, our proposed long-range hybrid single layer and bilayer NiO_2 planes in a single compound have been realized in $\text{La}_2\text{NiO}_4 \cdot \text{La}_3\text{Ni}_2\text{O}_7$, as evidenced by X-ray single crystal diffraction, Rietveld refinement on powder diffraction, and real-space imaging of the structure using STEM. In fact, this new compound just represents one member of a new family of long-range hybrid R-P nickelates. **Fig. 4a** shows the conventional R-P nickelates with the formula of $\text{La}_{n+1}\text{Ni}_n\text{O}_{3n+1}$ ($n=1, 2, 3, \dots, \infty$).²⁷ By expanding this R-P nickelate via introducing different building blocks, the hybrid R-P family of nickelates $\text{La}_{n+1}\text{Ni}_n\text{O}_{3n+1} \cdot \text{La}_{m+1}\text{Ni}_m\text{O}_{3m+1}$ ($m, n=1, 2, 3 \dots$ and $m>n$) can be formed as shown in **Fig. 4b**. Among them, $\text{La}_2\text{NiO}_4 \cdot \text{La}_3\text{Ni}_2\text{O}_7$ is the first member of this family with $n=1$ and $m=2$. By tuning conditions of materials synthesis during flux growth²⁰ or high pressure floating zone growth,²⁴ it is expected that $\text{La}_2\text{NiO}_4 \cdot \text{La}_4\text{Ni}_3\text{O}_{10}$ ($n=1, m=3$), $\text{La}_2\text{NiO}_4 \cdot \text{La}_5\text{Ni}_4\text{O}_{13}$ ($n=1, m=4$), $\text{La}_2\text{NiO}_4 \cdot \text{La}_6\text{Ni}_5\text{O}_{16}$ ($n=1, m=5$), $\text{La}_3\text{Ni}_2\text{O}_7 \cdot \text{La}_4\text{Ni}_3\text{O}_{10}$ ($n=2, m=3$), $\text{La}_3\text{Ni}_2\text{O}_7 \cdot \text{La}_5\text{Ni}_4\text{O}_{13}$ ($n=2, m=4$), $\text{La}_3\text{Ni}_2\text{O}_7 \cdot \text{La}_6\text{Ni}_5\text{O}_{16}$ ($n=2, m=5$), $\text{La}_4\text{Ni}_3\text{O}_{10} \cdot \text{La}_5\text{Ni}_4\text{O}_{13}$ ($n=3, m=4$), $\text{La}_4\text{Ni}_3\text{O}_{10} \cdot \text{La}_6\text{Ni}_5\text{O}_{16}$ ($n=3, m=5$), $\text{La}_5\text{Ni}_4\text{O}_{13} \cdot \text{La}_6\text{Ni}_5\text{O}_{16}$ ($n=4, m=5$), ... can be synthesized.

Even more nickelates can be designed and explored if one mixes different rare earth ions. Synthesis of these bulk samples may be challenging for $n, m>3$. As an alternative way, the preparation of thin films using techniques like molecular-beam epitaxy^{28,29} potentially have a better chance. **Fig. 4c** shows the general R-P phases $\text{A}_{n+1}\text{B}_n\text{X}_{3n+1} \cdot \text{A}'_{m+1}\text{B}'_m\text{X}'_{3m+1}$, where A and A' are usually alkaline earth or rare earth metal ion (e.g. Ca, Sr, Ba, La-Lu) or organic groups (e.g., CH_3NH_3 , $\text{CH}(\text{NH}_2)_2$), B and B' are transition metal ion (e.g. Ti, V, Mn, Fe, Co, Ni, Nb, Zr, Ru, Sn, Pb), X and X' are anion (e.g. O, Cl,

Br, I) and $m, n=1, 2, 3, \dots, \infty$. With the success of $\text{La}_2\text{NiO}_4 \cdot \text{La}_3\text{Ni}_2\text{O}_7$ in the nickelate system, it is straightforward to explore more general hybrid R-P phases in other transition metal oxides including cobaltites for spin transition,³⁰ manganites for colossal magnetoresistance,⁴ halide perovskites for photovoltaic applications³ and X-ray or γ -ray detection.^{31,32} Indeed, a superlattice of $\text{Sr}_2\text{IrO}_4 \cdot \text{Sr}_3\text{Ir}_2\text{O}_7$ with dimensions of a few microns in thickness, thicker than layer-by-layer grown thin films but thinner than typical bulk crystals, have been achieved,³³ and synthesis of bulk single crystals of this material and characterization of its physical properties are intriguing.

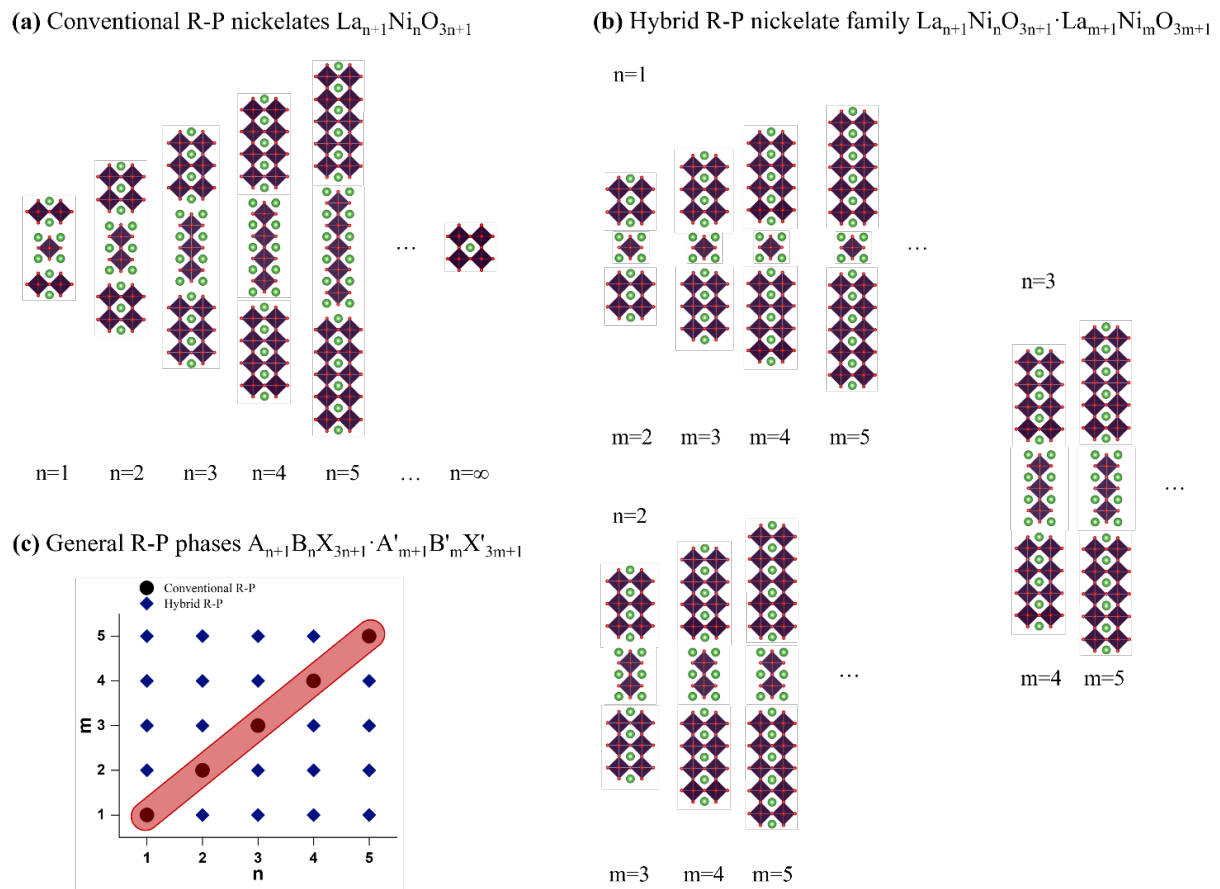


Figure 4. Hybrid Ruddlesden-Popper (R-P) phases as a new class of quantum materials that potentially host emerging physical properties. (a) Conventional R-P nickelates with the formula of $\text{La}_{n+1}\text{Ni}_n\text{O}_{3n+1}$ ($n=1, 2, 3, \dots$). Note n are integers and only one n exists in a single compound. (b) Hybrid R-P nickelate family with the formula of $\text{La}_{n+1}\text{Ni}_n\text{O}_{3n+1} \cdot \text{La}_{m+1}\text{Ni}_m\text{O}_{3m+1}$ ($m, n=1, 2, 3, \dots$ and $m \neq n$). $\text{La}_2\text{NiO}_4 \cdot \text{La}_3\text{Ni}_2\text{O}_7$ is one member of this family with $n=1$ and $m=2$. (c) General R-P phases with the formula of $\text{A}_{n+1}\text{B}_n\text{X}_{3n+1} \cdot \text{A}'_{m+1}\text{B}'_m\text{X}'_{3m+1}$ ($m, n=1, 2, 3, \dots$). In these compounds, A and A' are usually alkaline earth or rare earth metal ion (e.g. Ca, Sr, Ba, La-Lu) or organic groups (e.g., CH_3NH_3 , $\text{CH}(\text{NH}_2)_2$); B and B' are transition metal ion (e.g. Ti, V, Mn, Fe, Co, Ni, Nb, Zr, Ru, Sn, Pb); X and X' are anion (e.g. O, Cl, Br, I).

Furthermore, in the trilayer or bilayer R-P nickelates, the apical oxygen atoms between NiO₂ layers can be removed upon topotactical reduction,^{34,35} but the in-plane oxygen atoms remain unchanged, making La₂NiO₄·La₃Ni₂O₆ or La₂NiO₄·La₄Ni₃O₈ a unique system to explore R-P and the Ni-O planar (T'-structure) hybrid phase. For other members of the hybrid R-P nickelates (n>1, m>n), if succeed, it will be interesting to perform topotactical reduction to hybrid T'-structure nickelates for rich emergent physical properties such as charge order and high-*T_c* superconductivity.³⁶

In summary, by tailoring the bilayer NiO₂ from the recently discovered high-*T_c* superconductor La₃Ni₂O₇ and the single layer from the antiferromagnetic insulator La₂NiO₄, we have designed a long-range hybrid R-P nickelate La₂NiO₄·La₃Ni₂O₇. Realization of such a structure in real materials has been achieved via flux growth at ambient pressure. The crystal structure of La₂NiO₄·La₃Ni₂O₇ consists of single layers and bilayers stacking alternatively perpendicular to the ab plane as determined from single crystal X-ray diffraction. The structure is corroborated by Rietveld refinement on powder diffraction and confirmed by real-space imaging using STEM. This new material shows the Curie-Weiss behavior as indicated by magnetic susceptibility and a novel insulator-to-metal transition at low temperatures that has never been reported in nickelates. The discovery of La₂NiO₄·La₃Ni₂O₇ opens up horizons to a completely new family of hybrid R-P phases with the formula of A_{n+1}B_nX_{3n+1}·A'_{m+1}B'_mX'_{3m+1} (n ≠ m), which potentially host a plethora of emerging physical properties including high temperature superconductivity, colossal magnetoresistance, metal-insulator transition, multiferroicity and optoelectronic properties.

Note. During the preparation of this manuscript, we are informed that Chen et al. from Argonne National Laboratory successfully synthesized La₂NiO₄·La₄Ni₃O₁₀ (n=1, m=3) crystals and reported its crystal structure and resistivity measurement.³⁷ The existence of this nickelate phase is also reported by Puphal et al. by Germany group independently.³⁸ This so-called “1313” compound just serves as the second example of our proposed hybrid R-P family of nickelates.

Acknowledgements

Work at Shandong University was supported by the National Natural Science Foundation of China (12074219 and 12374457), the 111 Project 2.0 (BP2018013), the TaiShan Scholars Project of Shandong Province (tsqn201909031), the QiLu Young Scholars Program of Shandong University, the Crystalline Materials and Industrialization Joint Innovation Laboratory of Shandong University and

Shandong Institutes of Industrial Technology (Z1250020003), and the Project for Scientific Research Innovation Team of Young Scholars in Colleges and Universities of Shandong Province (2021KJ093). G. M. Zhang acknowledges the support of China's Ministry of Science and Technology (Grant No. 2023YFA1406400). J. Z. and F. L. thank Prof. Jian Zhang for his help with in-house single crystal X-ray diffraction. J.Z. thanks Dr. Yu-Sheng Chen and Dr. Tiejian Chang from The University of Chicago for stimulating discussions.

Author contributions

J.Z. and X.T. conceived the project and G.M. Z proposed the physical picture to design the hybrid RP family of materials. F.L. grew single crystals with the assistance of C.L. F.L. performed the powder and single-crystal X-ray diffraction experiments. F.L. performed SEM, EDS, magnetic susceptibility, and transport measurements with the help of Q.C. S.L.W., S.P.W. and C.L. N.G. and Q.Z. carried out STEM measurements and performed data analysis. F.L., J.Z., and G.M.Z. analyzed data. Y.S. performed DFT calculations with helps from G.M. Z. J.Z. and G.M. Z. wrote the manuscript with contributions from all coauthors.

Competing interests

The authors declare no conflict of interest.

References

- 1 Keimer, B., Kivelson, S. A., Norman, M. R., Uchida, S. & Zaanen, J. From quantum matter to high-temperature superconductivity in copper oxides. *Nature* **518**, 179-186 (2015).
- 2 Imada, M., Fujimori, A. & Tokura, Y. Metal-insulator transitions. *Rev. Mod. Phys.* **70**, 1039-1263 (1998).
- 3 Chen, Y. *et al.* 2D Ruddlesden–Popper Perovskites for Optoelectronics. *Adv. Mater.* **30**, 1703487 (2018). [https://doi.org:https://doi.org/10.1002/adma.201703487](https://doi.org/https://doi.org/10.1002/adma.201703487)
- 4 Salamon, M. B. & Jaime, M. The physics of manganites: Structure and transport. *Rev. Mod. Phys.* **73**, 583-628 (2001). <https://doi.org:10.1103/RevModPhys.73.583>
- 5 Lu, C., Wu, M., Lin, L. & Liu, J.-M. Single-phase multiferroics: new materials, phenomena, and physics. *Natl. Sci. Rev.* **6**, 653-668 (2019). <https://doi.org:10.1093/nsr/nwz091>
- 6 Xu, X., Pan, Y., Zhong, Y., Ran, R. & Shao, Z. Ruddlesden–Popper perovskites in electrocatalysis. *Materials Horizons* **7**, 2519-2565 (2020). <https://doi.org:10.1039/D0MH00477D>
- 7 Sloan, J., Battle, P. D., Green, M. A., Rosseinsky, M. J. & Vente, J. F. A HRTEM Study of the Ruddlesden–Popper Compositions $\text{Sr}_2\text{LnMn}_2\text{O}_7$ (Ln=Y, La, Nd, Eu, Ho). *J. Solid State Chem.* **138**, 135-140 (1998). <https://doi.org:https://doi.org/10.1006/jssc.1998.7764>

- 8 Hungria, T., MacLaren, I., Fuess, H., Galy, J. & Castro, A. HREM studies of intergrowths in $\text{Sr}_2[\text{Sr}_{n-1}\text{Ti}_n\text{O}_{3n+1}]$ Ruddlesden–Popper phases synthesized by mechanochemical activation. *Mater. Lett.* **62**, 3095-3098 (2008). [https://doi.org:https://doi.org/10.1016/j.matlet.2008.01.110](https://doi.org/10.1016/j.matlet.2008.01.110)
- 9 Ram, R. A. M., Ganapathi, L., Ganguly, P. & Rao, C. N. R. Evolution of three-dimensional character across the $\text{La}_{n+1}\text{Ni}_n\text{O}_{3n+1}$ homologous series with increase in n. *J. Solid State Chem.* **63**, 139-147 (1986). [https://doi.org:http://dx.doi.org/10.1016/0022-4596\(86\)90163-5](https://doi.org/http://dx.doi.org/10.1016/0022-4596(86)90163-5)
- 10 Park, C. & Snyder, R. L. Perovskite stacking in the structures of the high temperature cuprate superconductors. *Appl. Supercond.* **3**, 73-83 (1995). [https://doi.org:https://doi.org/10.1016/0964-1807\(95\)00035-4](https://doi.org:https://doi.org/10.1016/0964-1807(95)00035-4)
- 11 Oh, Y. S., Luo, X., Huang, F.-T., Wang, Y. & Cheong, S.-W. Experimental demonstration of hybrid improper ferroelectricity and the presence of abundant charged walls in $(\text{Ca},\text{Sr})_3\text{Ti}_2\text{O}_7$ crystals. *Nat. Mater.* **14**, 407-413 (2015). <https://doi.org:10.1038/nmat4168>
- 12 Zhang, J. & Tao, X. Review on quasi-2D square planar nickelates. *CrystEngComm* **23**, 3249-3264 (2021). <https://doi.org:10.1039/D0CE01880E>
- 13 Hücker, M. *et al.* Oxygen and strontium codoping of La_2NiO_4 : Room-temperature phase diagrams. *Phys. Rev. B* **70**, 064105 (2004).
- 14 Sun, H. L. *et al.* Signatures of superconductivity near 80 K in a nickelate under high pressure. *Nature* **621**, 493-498 (2023). <https://doi.org:10.1038/s41586-023-06408-7>
- 15 Yanan Zhang, D. S., Yanen Huang, Hualei Sun, Mengwu Huo, Zhaoyang Shan, Kaixin Ye, Zihan Yang, Rui Li, Michael Smidman, Meng Wang, Lin Jiao, Huiqiu Yuan. High-temperature superconductivity with zero-resistance and strange metal behavior in $\text{La}_3\text{Ni}_2\text{O}_7$. Preprint at <https://arxiv.org/abs/2307.14819> (2023).
- 16 Yazhou Zhou, J. G., Shu Cai, Hualei Sun, Pengyu Wang, Jinyu Zhao, Jinyu Han, Xintian Chen, Qi Wu, Yang Ding, Meng Wang, Tao Xiang, Ho-kwang Mao, Liling Sun. Evidence of filamentary superconductivity in pressurized $\text{La}_3\text{Ni}_2\text{O}_7$ single crystals. Preprint at <https://arxiv.org/abs/2311.12361> (2023).
- 17 J. Hou, P. T. Y., Z. Y. Liu, J. Y. Li, P. F. Shan, L. Ma, G. Wang, N. N. Wang, H. Z. Guo, J. P. Sun, Y. Uwatoko, M. Wang, G.-M. Zhang, B. S. Wang, J.-G. Cheng. Emergence of high-temperature superconducting phase in the pressurized $\text{La}_3\text{Ni}_2\text{O}_7$ crystals. Preprint at <https://arxiv.org/abs/2307.09865> (2023).
- 18 Zhang, J. *et al.* Large orbital polarization in a metallic square-planar nickelate. *Nat. Phys.* **13**, 864-869 (2017). <https://doi.org:10.1038/Nphys4149>
- 19 Klein, Y. M. *et al.* RENiO_3 Single Crystals (RE = Nd, Sm, Gd, Dy, Y, Ho, Er, Lu) Grown from Molten Salts under 2000 bar of Oxygen Gas Pressure. *Cryst. Growth Des.* **21**, 4230-4241 (2021). <https://doi.org:10.1021/acs.cgd.1c00474>
- 20 Li, F. *et al.* Flux Growth of Trilayer $\text{La}_4\text{Ni}_3\text{O}_{10}$ Single Crystals at Ambient Pressure. *Cryst. Growth Des.* (2023). <https://doi.org:10.1021/acs.cgd.3c01049>
- 21 Mingxin Zhang, C. P., Qi Wang, Yi Zhao, Changhua Li, Weizheng Cao, Shihao Zhu, Juefei Wu, Yanpeng Qi. Effects of Pressure and Doping on Ruddlesden–Popper phases. Preprint at <https://arxiv.org/abs/2309.01651> (2023).
- 22 Gang Wang, N. W., Yuxin Wang, Lifen Shi, Xiaoling Shen, Jun Hou, Hanming Ma, Pengtao Yang, Ziyi Liu, Hua Zhang, Xiaoli Dong, Jianping Sun, Bosen Wang, Kun Jiang, Jiangping Hu, Yoshiya Uwatoko, Jinguang Cheng. Observation of high-temperature superconductivity in the high-pressure tetragonal phase of $\text{La}_2\text{PrNi}_2\text{O}_{7-\delta}$. Preprint at <https://arxiv.org/abs/2311.08212>

- (2023).
- 23 Liu, Z. *et al.* Evidence for charge and spin density waves in single crystals of $\text{La}_3\text{Ni}_2\text{O}_7$ and $\text{La}_3\text{Ni}_2\text{O}_6$. *Sci. China-Phys. Mech. Astron.* **66**, 217411 (2023). <https://doi.org/10.1007/s11433-022-1962-4>
- 24 Zhang, J. *et al.* High oxygen pressure floating zone growth and crystal structure of the metallic nickelates $\text{R}_4\text{Ni}_3\text{O}_{10}$ (R=La, Pr). *Phys. Rev. Mater.* **4**, 083402 (2020). <https://doi.org/10.1103/PhysRevMaterials.4.083402>
- 25 Zhang, J. *et al.* Intertwined density waves in a metallic nickelate. *Nat. Commun.* **11**, 6003 (2020). <https://doi.org/10.1038/s41467-020-19836-0>
- 26 Catalano, S. *et al.* Rare-earth nickelates RNiO_3 : thin films and heterostructures. *Rep. Prog. Phys.* **81**, 046501 (2018).
- 27 Greenblatt, M. Ruddlesden-popper $\text{Ln}_{n+1}\text{Ni}_n\text{O}_{3n+1}$ nickelates: Structure and properties. *Curr. Opin. Solid State Mater. Sci.* **2**, 174-183 (1997).
- 28 Pan, G. A. *et al.* Synthesis and electronic properties of $\text{Nd}_{n+1}\text{Ni}_n\text{O}_{3n+1}$ Ruddlesden-Popper nickelate thin films. *Phys. Rev. Mater.* **6**, 055003 (2022). <https://doi.org/10.1103/PhysRevMaterials.6.055003>
- 29 Song, J. *et al.* Synergistic Role of Eg Filling and Anion–Cation Hybridization in Enhancing the Oxygen Evolution Reaction Activity in Nickelates. *ACS Applied Energy Materials* **4**, 12535-12542 (2021). <https://doi.org/10.1021/acsaem.1c02335>
- 30 Raveau, B. & Seikh, M. M. *Cobalt oxides: from crystal chemistry to physics.* (Wiley-VCH Verlag & Co. KGaA, 2012).
- 31 Han, M. *et al.* Recent advances on two-dimensional metal halide perovskite x-ray detectors. *Materials Futures* **2**, 012104 (2023). <https://doi.org/10.1088/2752-5724/acba36>
- 32 Liu, F. *et al.* Recent Progress in Halide Perovskite Radiation Detectors for Gamma-Ray Spectroscopy. *Acs Energy Lett* **7**, 1066-1085 (2022). <https://doi.org/10.1021/acsenergylett.2c00031>
- 33 Kim, H. *et al.* $\text{Sr}_2\text{NiO}_4/\text{Sr}_3\text{Ir}_2\text{O}_7$ superlattice for a model two-dimensional quantum Heisenberg antiferromagnet. *Phys. Rev. Research* **4**, 013229 (2022). <https://doi.org/10.1103/PhysRevResearch.4.013229>
- 34 Lacorre, P. Passage from T-type to T'-type arrangement by reducing $\text{R}_4\text{Ni}_3\text{O}_{10}$ to $\text{R}_4\text{Ni}_3\text{O}_8$ (R = La, Pr, Nd). *J. Solid State Chem.* **97**, 495-500 (1992).
- 35 Poltavets, V. V. *et al.* $\text{La}_3\text{Ni}_2\text{O}_6$: a new double T'-type nickelate with infinite $\text{Ni}^{1+/2+}\text{O}_2$ layers. *J. Am. Chem. Soc.* **128**, 9050-9051 (2006).
- 36 Li, D. *et al.* Superconductivity in an infinite-layer nickelate. *Nature* **572**, 624-627 (2019). <https://doi.org/10.1038/s41586-019-1496-5>
- 37 Xinglong Chen, J. Z., A.S. Thind, S. Sharma, H. LaBollita, G. Peterson, H. Zheng, D. Phelan, A.S. Botana, R.F. Klie, J.F. Mitchell. Polymorphism in Ruddlesden-Popper $\text{La}_3\text{Ni}_2\text{O}_7$: Discovery of a Hidden Phase with Distinctive Layer Stacking. Preprint at <https://arxiv.org/abs/2312.06081> (2023).
- 38 Pascal Puphal, P. R., Niklas Enderlein, Yu-Mi Wu, Giniyat Khaliullin, Vignesh Sundaramurthy, Tim Priessnitz, Manuel Knauff, Lea Richter, Masahiko Isobe, Peter A. van Aken, Hidenori Takagi, Bernhard Keimer, Y. Eren Suyolcu, Björn Wehinger, Philipp Hansmann, Matthias Hepting. Unconventional crystal structure of the high-pressure superconductor $\text{La}_3\text{Ni}_2\text{O}_7$. Preprint at <https://arxiv.org/abs/2312.07341> (2023).

- 39 Computer code APEX4 (Bruker Analytical X-ray Instruments, Inc. Madison, Wisconsin, USA., 2022).
- 40 Dolomanov, O. V., Bourhis, L. J., Gildea, R. J., Howard, J. A. K. & Puschmann, H. OLEX2: a complete structure solution, refinement and analysis program. *J. Appl. Crystallogr.* **42**, 339-341 (2009). <https://doi.org:doi:10.1107/S0021889808042726>
- 41 Blöchl, P. E. Projector augmented-wave method. *Phys. Rev. B* **50**, 17953-17979 (1994). <https://doi.org:10.1103/PhysRevB.50.17953>
- 42 Kresse, G. & Furthmüller, J. Efficient iterative schemes for ab initio total-energy calculations using a plane-wave basis set. *Phys. Rev. B* **54**, 11169-11186 (1996). <https://doi.org:10.1103/PhysRevB.54.11169>
- 43 Kresse, G. & Joubert, D. From ultrasoft pseudopotentials to the projector augmented-wave method. *Phys. Rev. B* **59**, 1758-1775 (1999). <https://doi.org:10.1103/PhysRevB.59.1758>
- 44 Perdew, J. P., Burke, K. & Ernzerhof, M. Generalized gradient approximation made simple. *Phys. Rev. Lett.* **77**, 3865-3868 (1996).
- 45 Dudarev, S. L., Botton, G. A., Savrasov, S. Y., Humphreys, C. J. & Sutton, A. P. Electron-energy-loss spectra and the structural stability of nickel oxide: An LSDA+U study. *Phys. Rev. B* **57**, 1505-1509 (1998). <https://doi.org:10.1103/PhysRevB.57.1505>

Experimental Section

Single crystal growth. Single crystals of $\text{La}_2\text{NiO}_4 \cdot \text{La}_3\text{Ni}_2\text{O}_7$ were grown for the first-time using flux method with K_2CO_3 as a flux at ambient pressure. Mixture of preheated La_2O_3 (Sigma-Aldrich, 99.99%), Ni (Alfa Aesar, 99.8%, particle size 5-15 μm) and anhydrous K_2CO_3 (Aladdin, 99.99%) in the molar ratio of 5:6:210 were loaded in a Al_2O_3 crucible with a lid in order to minimize the evaporation. The procedure for crystal growth is similar to that of $\text{La}_4\text{Ni}_3\text{O}_{10}$.²⁰

X-ray diffraction. Single crystal X-ray diffraction data were collected using a Bruker AXS D8 Venture (Mo- $K\alpha_1$ radiation, $\lambda = 0.71073 \text{ \AA}$) diffractometer at room temperature. A single crystal with dimensions of $40 \times 57 \times 58 \mu\text{m}^3$ was used to determine the structure of $\text{La}_2\text{NiO}_4 \cdot \text{La}_3\text{Ni}_2\text{O}_7$. For data collection, Ω and Φ scans were used, and 2728 frames were collected. Indexing was performed using Bruker APEX4 software.³⁹ Data integration and cell refinement were performed using SAINT, and multiscan absorption corrections were applied using the SADABS program.³⁹ Using Olex2,⁴⁰ the structure was solved with the XT structure solution program using Intrinsic Phasing and refined with the XL refinement package using Least Squares minimisation.³⁹ All La and Ni atoms (except O atoms) were modeled using anisotropic ADPs, and the refinements converged for $I > 2\sigma(I)$, where I is the intensity of reflections and $\sigma(I)$ is standard deviation. Further details of the crystal structure investigations may be obtained from the joint CCDC/FIZ Karlsruhe online deposition service by quoting the deposition number CSD 2313044. Powder X-ray powder diffraction data were collected on a Bruker AXS D2 Phaser diffractometer at room temperature using Cu- $K\alpha$ radiation ($\lambda = 1.5418 \text{ \AA}$) in the 2θ range of $10\text{-}140^\circ$ with a scan step size of 0.01° and a scan time of 2.1 s per step. TOPAS 6 was used for Rietveld refinement where single-crystal structural model was used as a starting model. Refinement parameters include background (chebychev function, order 5), sample displacement, lattice parameters, crystallite size L and strain G .

Scanning Electron Microscopy (SEM). The morphology of the as-grown crystals was examined using a scanning electron microscope. The scanning electron microscope images were obtained by Hitachi S-4800 microscope incident electron of 5.0 kV.

Energy Dispersive Spectrometer (EDS). The X-ray spectrometer EDAX GENESIS XM2 SYSTEM 60x on S-4800 was used for qualitative and quantitative analysis of the as-grown crystals. The experiments were carried out on three single crystals.

Scanning transmission electron microscopy (STEM). STEM specimens were prepared by crushing $\text{La}_2\text{NiO}_4 \cdot \text{La}_3\text{Ni}_2\text{O}_7$ single crystals in ethanol. A drop of the suspensions was deposited on lacey carbon-coated copper grids and dried in air. High-angle annular dark-field (HAADF)-STEM images were acquired at an accelerating voltage of 300 kV on a double-aberration-corrected transmission

electron microscope (Spectra 300, Thermo Fisher Scientific), equipped with a field-emission electron source. The probe convergence semi-angle and inner collection semi-angle are 25.0 mrad and 49 mrad, respectively. Energy dispersive spectroscopy (EDS) data were obtained with a Super-X EDS detector.

Resistivity. The resistivity of $\text{La}_2\text{NiO}_4 \cdot \text{La}_3\text{Ni}_2\text{O}_7$ was measured using the standard four-probe method on polycrystalline pellets under an external magnetic field of 0 and 5 T. Note a single crystal is too small to put four leads on, polycrystalline pellets were used and treated at 900 °C in air prior to making contacts with silver paste. A Quantum Design Physical Property Measurement System (DynaCool-9) was used to measure resistivity in the temperature range of 2-300 K at a warming rate of 3.0 K/min.

Magnetic susceptibility. DC magnetization of as-grown $\text{La}_2\text{NiO}_4 \cdot \text{La}_3\text{Ni}_2\text{O}_7$ single crystals was measured using a PPMS DynaCool 9 T. ZFC-W (zero-field cooling with data collected on warming), FC-C (field cooling and data collected on cooling), and FC-W (field cooling and data collected on warming) data were collected between 2 and 300 K under an external magnetic field of 0.4 T. After cooled to 2 K under zero magnetic field, data were collected on warming at a rate of 3 K/min. FC-C and FC-W data collection used the same rate of 3 K/min.

DFT calculations. The first-principles calculations were performed with the density functional theory using the projector augmented wave (PAW) method⁴¹ implemented in the Vienna Ab Initio Simulation Package (VASP).^{42,43} The exchange correlation potential is described by generalized gradient approximation (GGA) of Perdew-Burke-Ernzerhof (PBE) functions.⁴⁴ Strong electron-electron correlation beyond GGA for nickel 3*d* electrons is supplemented by plus Hubbard *U* (GGA + *U*) calculations with Dudarev's approach,⁴⁵ and we take $U = 4$ eV in this work. An energy cutoff of 600 eV for the plane-wave expansion and a $7 \times 6 \times 1$ Monkhorst-Pack grid for *k*-point sampling are adopted for self-consistent calculations with good convergence (with accuracy at 10^{-6} eV). The crystal structure was fixed to the experimentally refined lattice constants obtained from SXRD.

Supplementary Materials for:

Design and synthesis of three-dimensional hybrid Ruddlesden-Popper nickelate single crystals

Feiyu Li,¹ Ning Guo,² Qiang Zheng,² Yang Shen,³ Shilei Wang,¹ Qihui Cui,¹ Chao Liu,¹ Shanpeng Wang,¹ Xutang Tao,^{1*} Guang-Ming Zhang,^{4,5*} Junjie Zhang^{1*}

¹State Key Laboratory of Crystal Materials and Institute of Crystal Materials, Jinan, Shandong 250100, China

²CAS Key Laboratory of Standardization and Measurement for Nanotechnology, CAS Center for Excellence in Nanoscience, National Center for Nanoscience and Technology, Beijing, 100190 China

³Key Laboratory of Artificial Structures and Quantum Control, School of Physics and Astronomy, Shanghai Jiao Tong University, Shanghai 200240, China

⁴State Key Laboratory of Low-Dimensional Quantum Physics, Department of Physics, Tsinghua University, Beijing, China.

⁵Frontier Science Center for Quantum Information, Beijing 10008, China

*Email: jingt535tao@163.com (X. Tao), gmzhang@mail.tsinghua.edu.cn (G. M. Zhang), and

junjie@sdu.edu.cn (J. Zhang)

Figure S1. A photo of as-grown single crystals of $\text{La}_2\text{NiO}_4 \cdot \text{La}_3\text{Ni}_2\text{O}_7$ using flux method.

Figure S2. Initial determination of unit cell using APEX3.

Figure S3. Calculated structural factor using the Immm model as a function of observed structural factor from the single crystal X-ray diffraction data.

Table S1. Crystal data and structure refinement for $\text{La}_2\text{NiO}_4 \cdot \text{La}_3\text{Ni}_2\text{O}_7$.

Figure S4. Real-space imaging of $\text{La}_2\text{NiO}_4 \cdot \text{La}_3\text{Ni}_2\text{O}_7$ in the projection of [110].

Figure S5. Real-space imaging of $\text{La}_2\text{NiO}_4 \cdot \text{La}_3\text{Ni}_2\text{O}_7$ in the projection of [100].

Figure S6. Real-space imaging of $\text{La}_2\text{NiO}_4 \cdot \text{La}_3\text{Ni}_2\text{O}_7$ in the projection of [100] with lower-magnification.

Figure S7. DFT+ U band structure calculations of non-magnetic $\text{La}_2\text{NiO}_4 \cdot \text{La}_3\text{Ni}_2\text{O}_7$. Orbital projected weights from all Ni 3d orbitals and all O 2p orbitals.

Figure S8. DFT+ U band structure calculations of non-magnetic $\text{La}_2\text{NiO}_4 \cdot \text{La}_3\text{Ni}_2\text{O}_7$. Orbital projected weights from La 5d orbitals compared to O 2p orbitals, indicating the presence of charge transfer via the LaO chains between the bilayer and monolayer of nickel oxide planes within the unit cell.

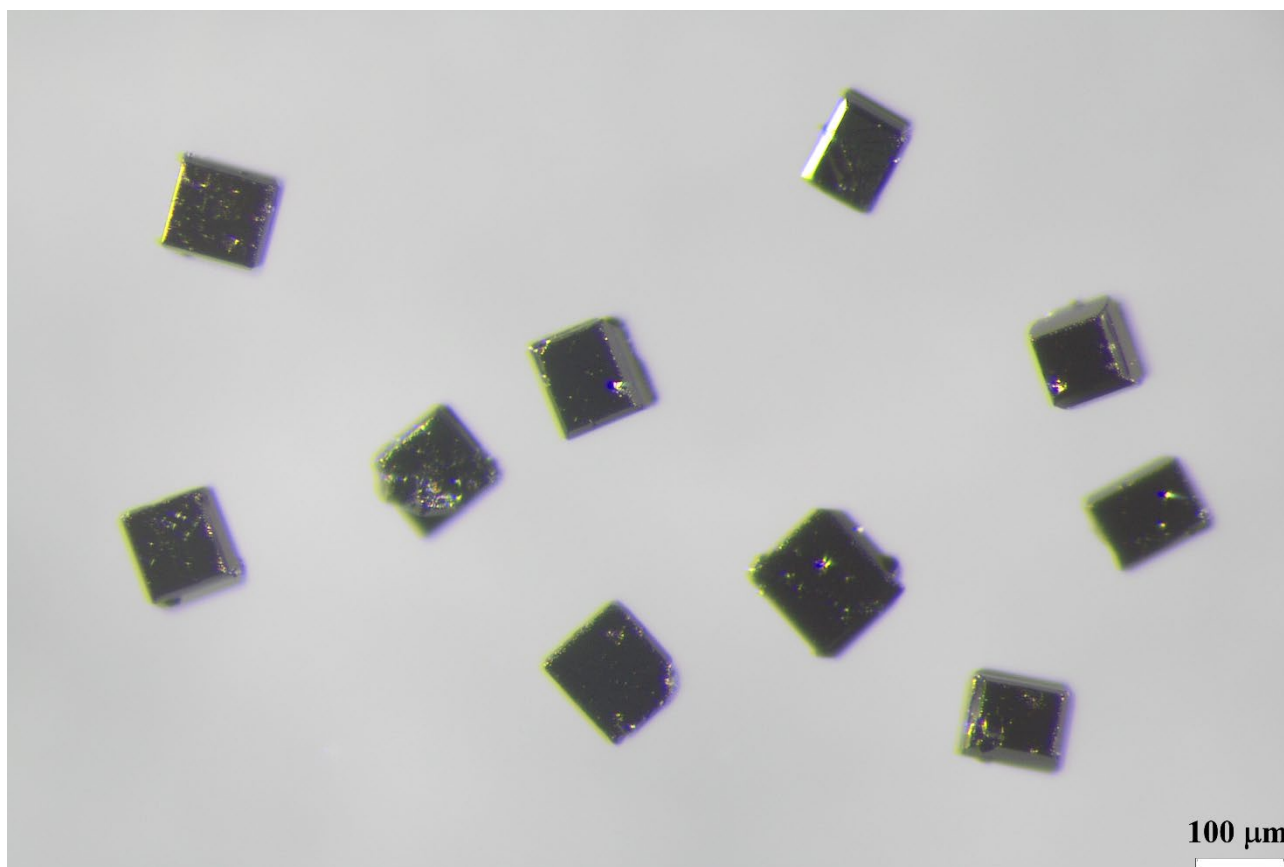
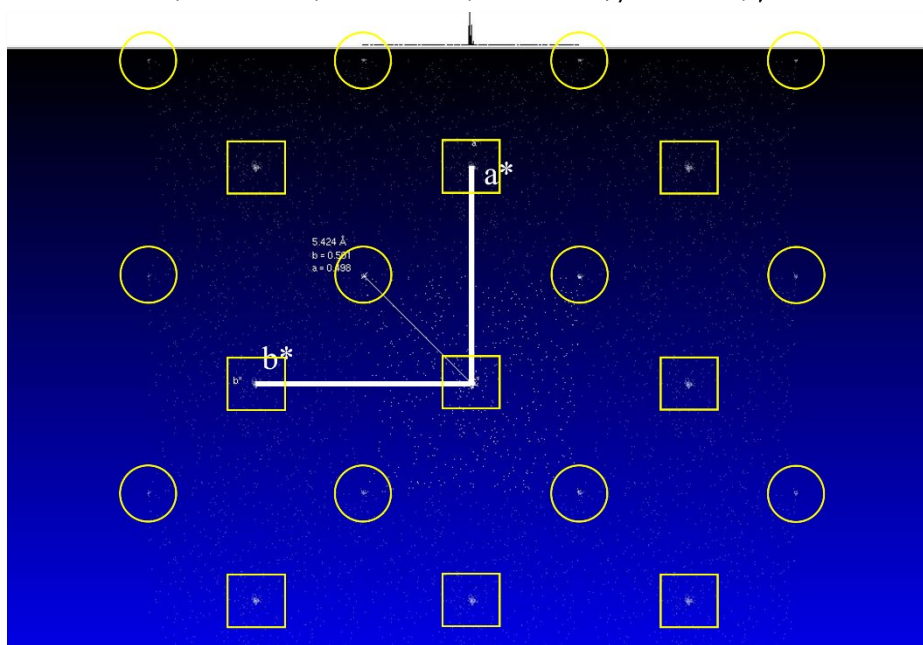


Figure S1. A photo of as-grown single crystals of $\text{La}_2\text{NiO}_4 \cdot \text{La}_3\text{Ni}_2\text{O}_7$ using flux method. The typically dimensions of single crystals are 100-120 μm in length and width and 30-50 μm in thickness.

- (a) a^*b^* plane in the reciprocal space
 $a=3.84 \text{ \AA}$, $b=3.84 \text{ \AA}$, $c=16.55 \text{ \AA}$, $\alpha=89.98^\circ$, $\beta=89.99^\circ$, $\gamma=90.06^\circ$



- (b) a^*c^* plane in the reciprocal space

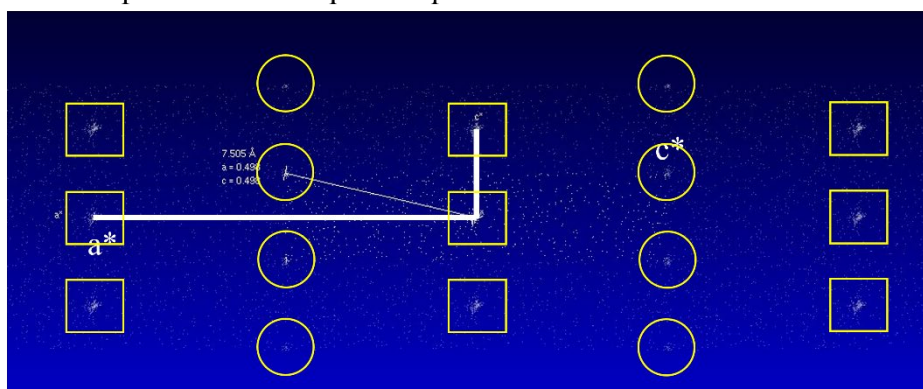


Figure S2. Initial determination of unit cell in the reciprocal space using APEX3. (a) Reflections with a wavevector of $(1/2, 1/2, 0)$ as marked by circles are clearly seen using the orthorhombic setting with $a \sim 3.83 \text{ \AA}$, $b \sim 3.83 \text{ \AA}$ and $c \sim 16.55 \text{ \AA}$. This indicates the unit cell should be twice large, i.e., $a \sim 5.4 \text{ \AA}$, $b \sim 5.4 \text{ \AA}$. (b) Reflections with a wavevector of $(1/2, 0, 1/2)$ are clearly seen using the orthorhombic setting with $a \sim b \sim 3.83$ and $c \sim 16.55$. This indicates the c axis should be doubled. Finally, the correct unit cell is orthorhombic with $a = 5.4296(2) \text{ \AA}$, $b = 5.4330(2) \text{ \AA}$, $c = 33.2067(12) \text{ \AA}$.

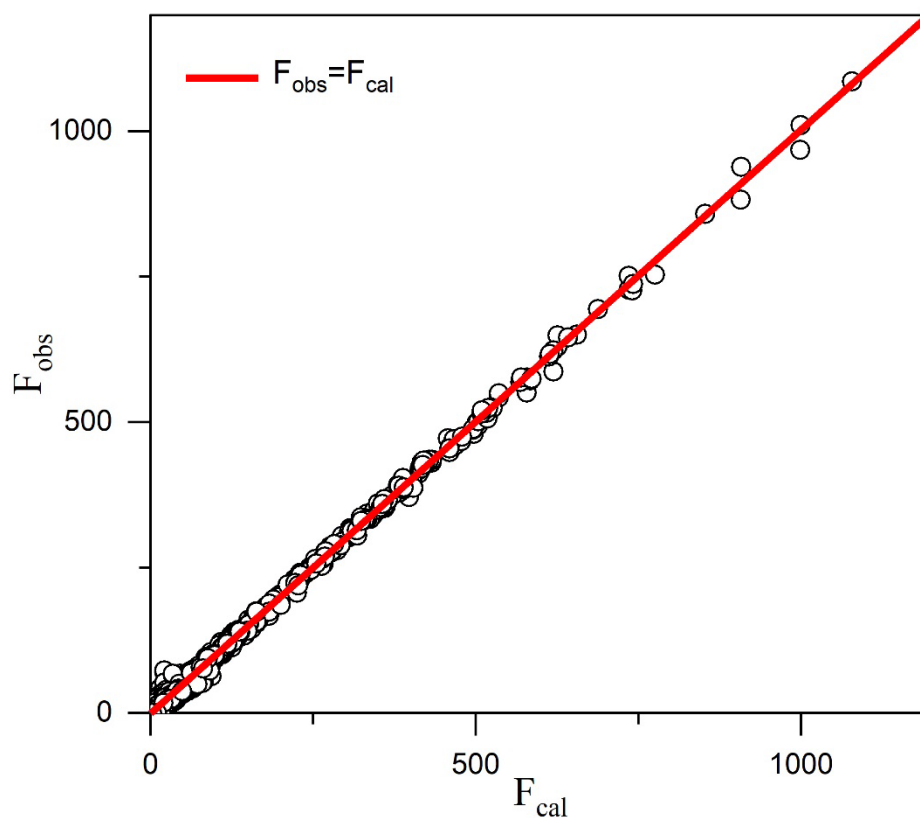


Figure S3. Calculated structural factor using the *Immm* model as a function of observed structural factor from the single crystal X-ray diffraction data. The observed structural factor F as a function of calculated F with the red line of $F_{\text{cal}}=F_{\text{obs}}$. The intensity is proportional to F^2 .

Table S1. Crystal data and structure refinement for $\text{La}_2\text{NiO}_4 \cdot \text{La}_3\text{Ni}_2\text{O}_7$.

Empirical formula	$\text{La}_2\text{NiO}_4 \cdot \text{La}_3\text{Ni}_2\text{O}_7$
Formula weight	1046.68
Temperature	296(2) K
Wavelength	0.71073 Å
Crystal system	orthorhombic
Space group	<i>Immm</i>
Unit cell dimensions	$a = 5.4296(2)$ Å $b = 5.4330(2)$ Å $c = 33.2067(12)$ Å
volume	$979.57(6)$ Å ³
Z	4
Density(calculated)	7.097 g/cm ³
Absorption coefficient	26.978 mm ⁻¹
$F(000)$	1828.0
Crystal size	0.058×0.057×0.040 mm ³
Radiation	MoK α ($\lambda = 0.71073$ Å)
2 Θ range for data collection/°	4.906 to 72.672
Index range	$-9 \leq h \leq 8, -9 \leq k \leq 9, -55 \leq l \leq 55$
Reflections collected	22488
Independent reflections	1404 [$R_{\text{int}}=4.11\%$, $R_{\text{sigma}}=1.70\%$]
Absorption correction	multi-scan
Refinement method	Full-matrix least-squares on F^2
Data/ restraints/ parameters	1404 / 0 / 51
Goodness-of-fit on F^2	1.164
Final R indices [$I > 2\sigma(I)$]	$R_1=6.05\%$, $wR_2=10.23\%$
R indices (all data)	$R_1=7.68\%$, $wR_2=11.12\%$
Largest diff. peak and hole	9.96 and -6.29 e. Å ³

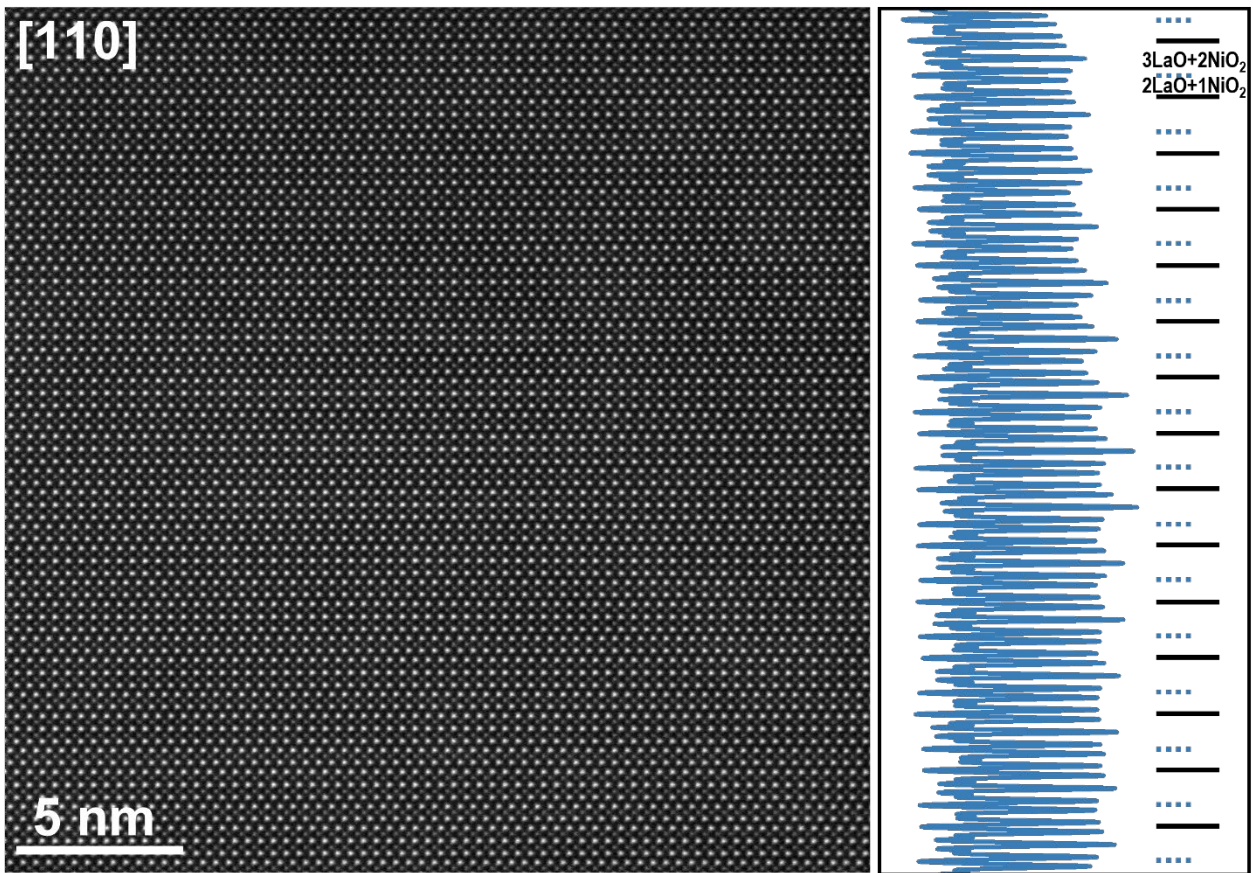


Figure S4. Real-space imaging of $\text{La}_3\text{Ni}_2\text{O}_7 \cdot \text{La}_2\text{NiO}_4$ in the projection of $[110]$. Lower-magnification HAADF-STEM image in the projection of $[110]$ is shown, the right panel is line intensity profile for rows of all atomic columns. Lower-magnification HAADF-STEM image in the projection of $[110]$ verifies the perfectly ordered stacking of alternating bilayers and single layers.

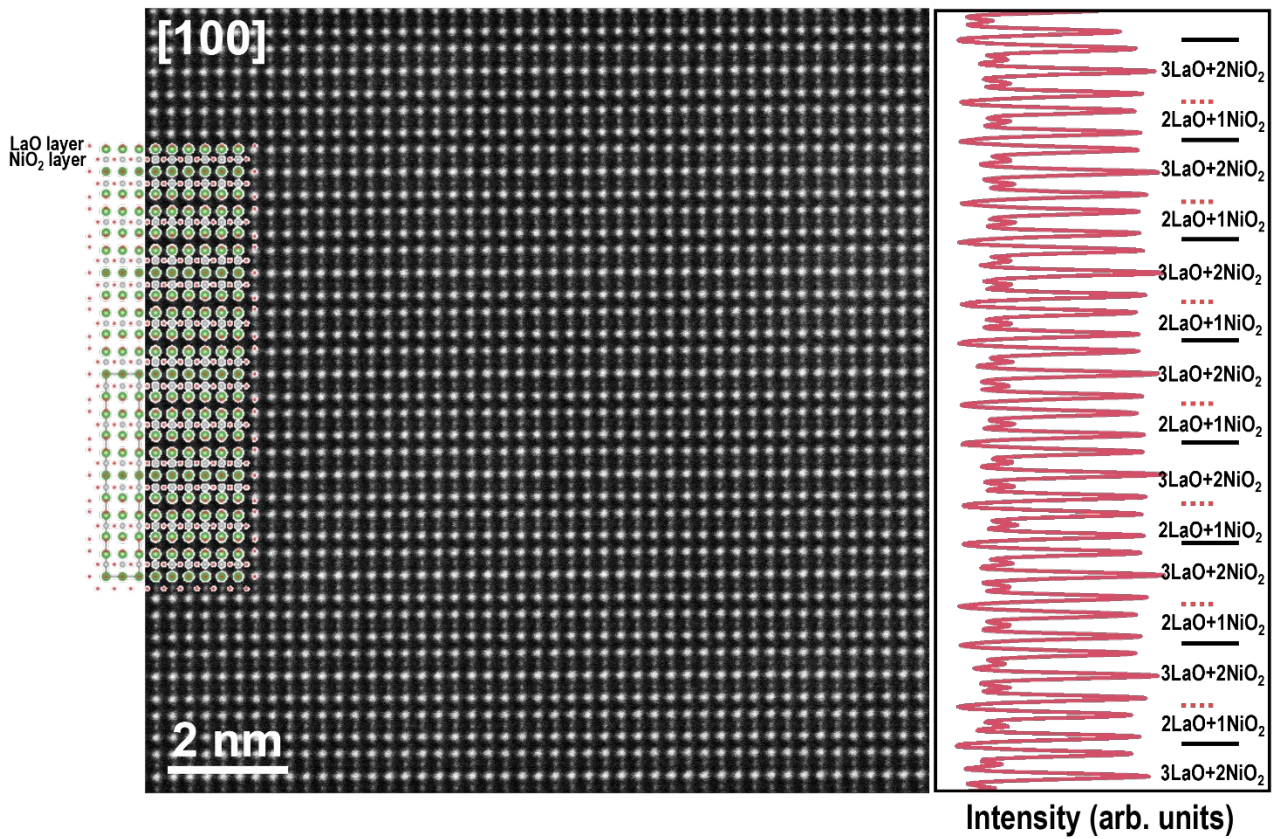


Figure S5. Real-space imaging of $\text{La}_3\text{Ni}_2\text{O}_7 \cdot \text{La}_2\text{NiO}_4$ in the projection of $[100]$. Stacking of alternating bilayers and single layers is revealed by HAADF-STEM image. The crystal structure model of $\text{La}_3\text{Ni}_2\text{O}_7 \cdot \text{La}_2\text{NiO}_4$ is overlaid on the image; the right panel is line intensity profile for rows of all atomic columns.

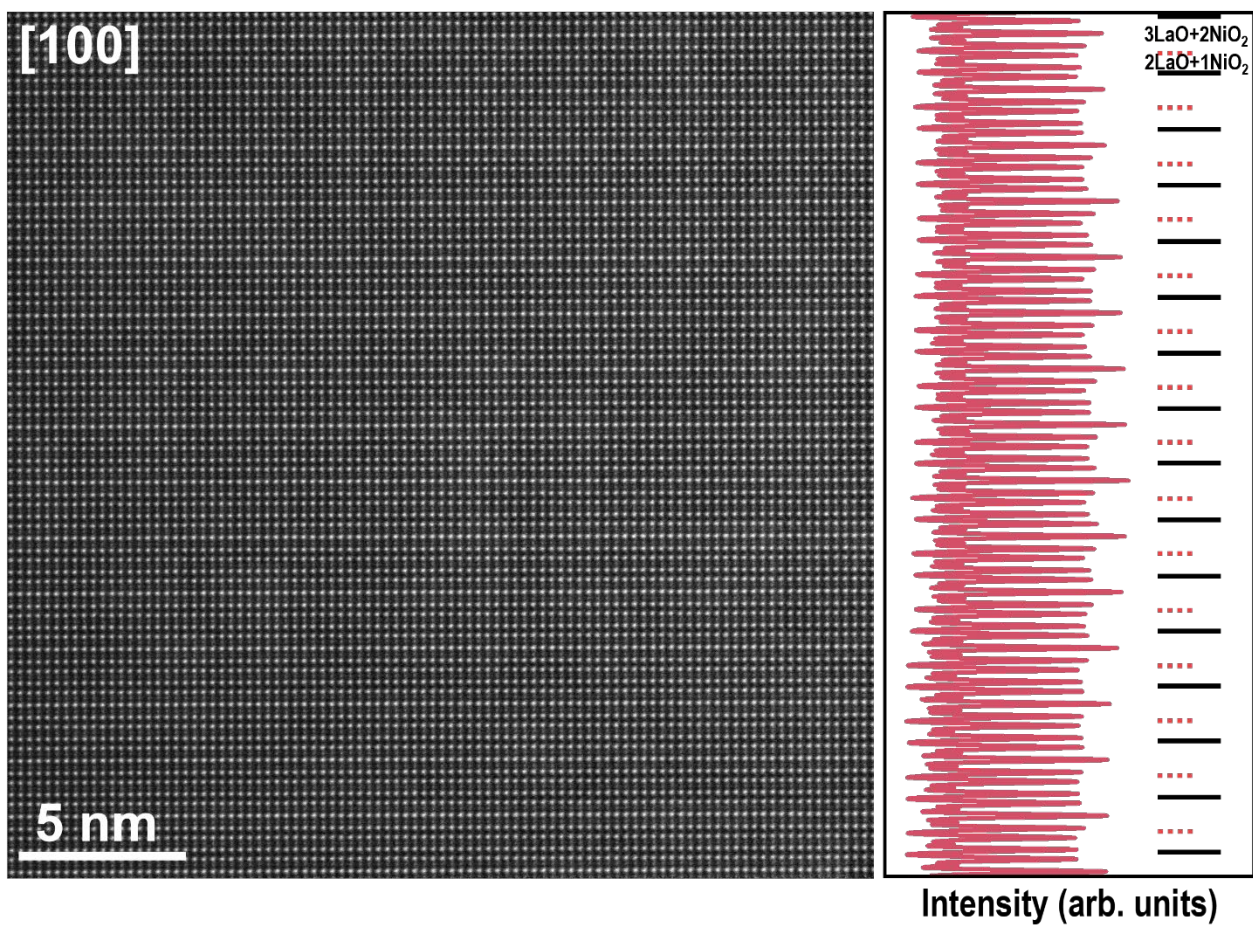


Figure S6. Real-space imaging of $\text{La}_3\text{Ni}_2\text{O}_7 \cdot \text{La}_2\text{NiO}_4$ in the projection of $[100]$ with lower-magnification. Lower-magnification HAADF-STEM image in the projection of $[100]$ verifies the perfectly ordered stacking of alternating bilayers and single layers. The right panel is line intensity profile for rows of all atomic columns.

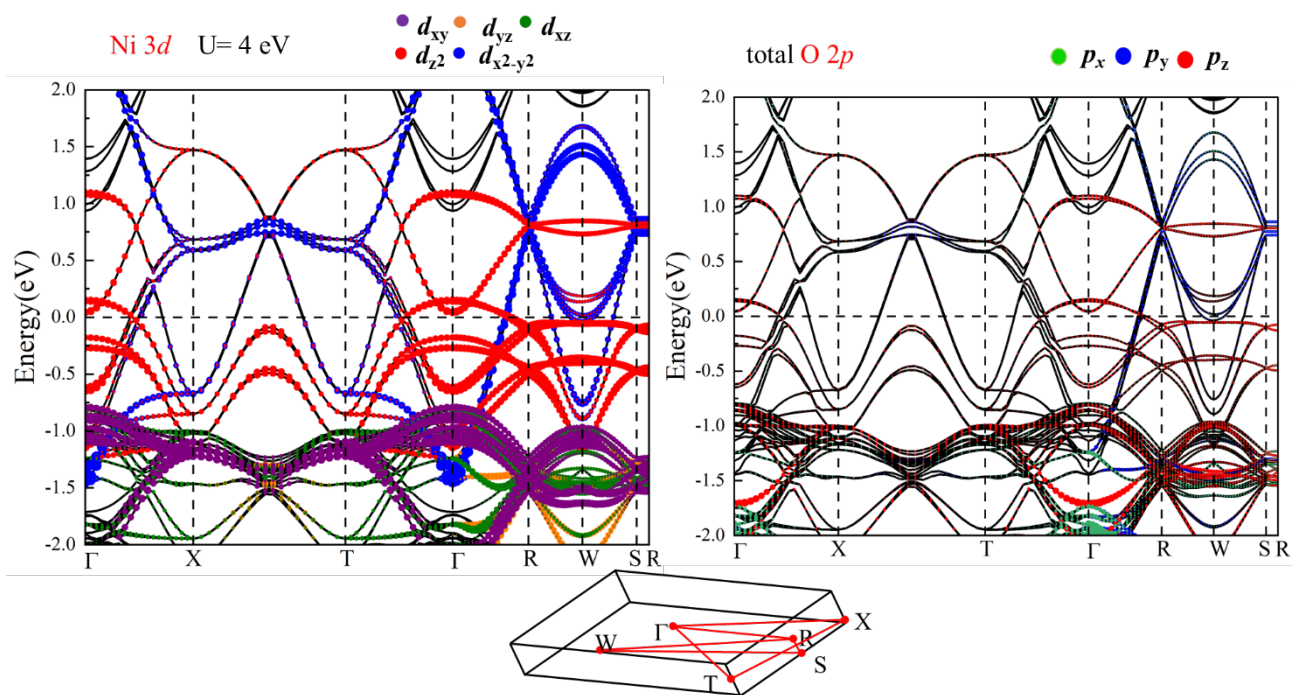


Figure S7. DFT+ U band structure calculations of non-magnetic $\text{La}_2\text{NiO}_4 \cdot \text{La}_3\text{Ni}_2\text{O}_7$. Orbital projected weights from (a) all Ni 3d orbitals and (b) all O 2p orbitals.

$U=4$ eV

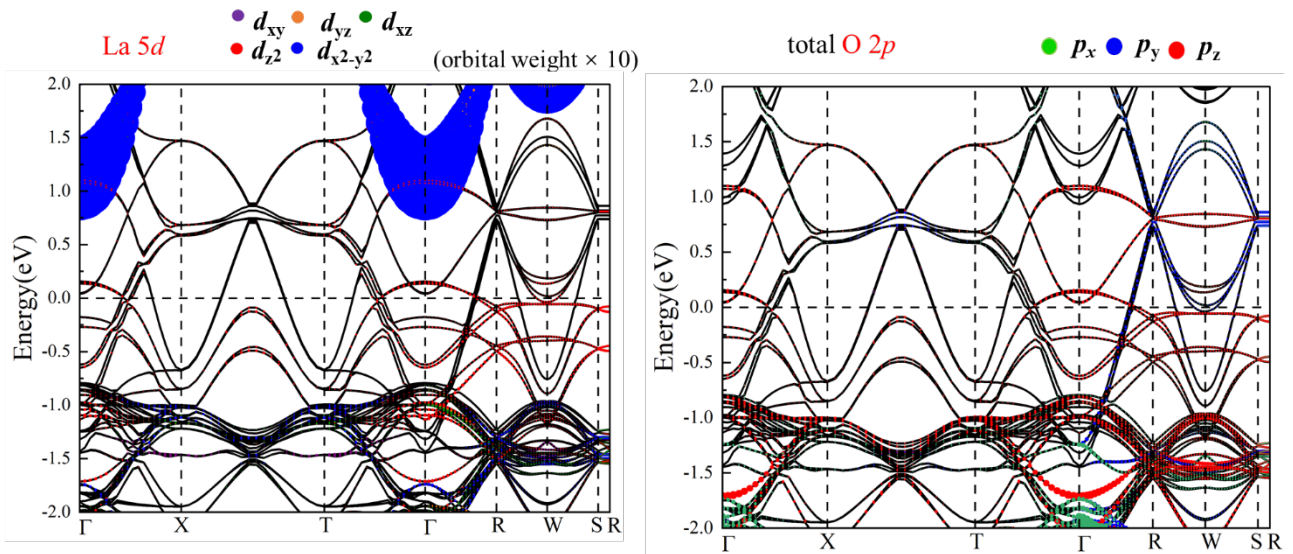


Figure S8. DFT+ U band structure calculations of non-magnetic $\text{La}_2\text{NiO}_4\cdot\text{La}_3\text{Ni}_2\text{O}_7$. Orbital projected weights from La 5d orbitals. Notice that the orbital weight of La 5d orbitals is ten times as large as other orbitals. Compared to O 2p orbitals, it indicates the presence of charge transfer via the LaO chains between the bilayer and mono-layer of nickel oxide planes within the unit cell.